Journal of Controlled Release 172 (2013) 118–127

Contents lists available at ScienceDirect

Journal of Controlled Release

journal homepage: www.elsevier.com/locate/jconrel

SPIO nanoparticle-stabilized PAA-F127 thermosensitive nanobubbles with MR/US dual-modality imaging and HIFU-triggered drug release for magnetically guided *in vivo* tumor therapy

Hsin-Yang Huang [a], Shang-Hsiu Hu [b], Shih-Ya Hung [a], Chih-Sheng Chiang [a], Hao-Li Liu [c], Tsung-Lang Chiu [d], Hsin-Yi Lai [e], You-Yin Chen [f,*], San-Yuan Chen [a,*]

[a] Department of Materials Science and Engineering, National Chiao Tung University, No. 1001, Ta-Hsueh Rd., Hsinchu 300, Taiwan, ROC
[b] Department of Biomedical Engineering and Environmental Sciences, National Tsing Hua University, Hsinchu 300, Taiwan, ROC
[c] Departments of Electrical Engineering, Chang-Gung University College of Medicine and Memorial Hospital, Taoyuan 333, Taiwan, ROC
[d] Department of Neurosurgery, Tzu Chi General Hospital, Tzu Chi University, No. 707, Sec. 3, Chung Yang Rd., Hualien 970, Taiwan, ROC
[e] Department of Neurology, University of North Carolina at Chapel Hill, No.130 Mason Farm Rd., CB# 7513, Chapel Hill 27599, USA
[f] Department of Biomedical Engineering, National Yang Ming University, No.155, Sec. 2, Linong St., Taipei 112, Taiwan, ROC

ARTICLE INFO

Article history:
Received 19 March 2013
Accepted 29 July 2013
Available online 9 August 2013

Keywords:
Magnetic targeting
Focus ultrasound
Superparamagnetic
Nanobubble

ABSTRACT

Nanobubbles can serve as promising, next-generation theranostic platforms for ultrasound (US) and magnetic resonance (MR) imaging, and combined magnetic targeting (MT) and high-intensity focused ultrasound (HIFU)-triggered drug release for tumor therapy. Nanobubble-based dual contrast enhancement agents encapsulated with perfluoropentane and stabilized with superparamagnetic iron oxide (SPIO) nanoparticles have been synthesized through a single-step emulsion process from thermosensitive F127 and polyacrylic acid (PAA). Both US and MR imaging contrast can be optimized by varying the shell thickness and SPIO-embedded concentration. The US contrast can be enhanced from a mean gray value of 62 to 115, and the MR r_2 value can be enhanced from 164 to 208 (s^{-1} mM^{-1} Fe) by increasing the SPIO concentration from 14.1 to 28.2 mg/mL, respectively. *In vivo* investigations of SPIO-embedded nanobubbles in excised tumors under external MT revealed that the US and MR signals change quantitatively compared to the same site without MT. This combined strategy enables the nanobubbles to enhance both passive targeting (increasing the permeability by HIFU) and physical MT of chemotherapeutic drugs to tumors. The integration of functionalities makes this nanobubble system a powerful and viable new tool to achieve simultaneous *in vivo* tumor imaging and efficacious cancer therapy.

1. Introduction

Employing theranostic nanoparticles, which combine both therapeutic and diagnostic capabilities in a single probe, has moved nanomedicine towards a new era of more effective and personalized treatment approaches, especially for tumor therapy and imaging. The ultrasound (US) technique has become friendly and easy-to-use as a diagnostic tool in clinical applications, and US is easy to focus and penetrates deep into soft tissue in a noninvasive manner. Moreover, US has been demonstrated to enhance the intercellular uptake of drugs and trigger the release of drugs [1,2], but US has exhibited a poor deep tissue discrimination ability because of its image resolution [3,4]. In contrast, magnetic resonance (MR) imaging is routinely used clinically during the preparation phase and for post-treatment evaluation because MR imaging is a powerful, noninvasive technique for obtaining real-time images that contain morphological and functional information with high resolution at the cellular and molecular levels. Superparamagnetic iron oxide (SPIO) nanoparticles and stabilized gas microbubbles (MBs) [5,6] are used as contrast agents for MR and US imaging, respectively. However, for the nanotheranostic treatment of various diseases, particularly cancers, it is essential to develop drug-loaded, nanosized contrast agents that take advantage of the inherent size of the nanoparticles and of the unique properties of tumor vasculature through the enhanced permeability and retention (EPR) effect, which allows nanobubbles to pass into the extravascular spaces and accumulate inside tumors [7]. Therefore, further innovations in the development of a drug nanocarrier that possesses the advantage of MR and US dual-modality imaging and the US-triggered release of therapeutic agents to tumor cells may offer a new type of therapeutic application [8,9].

Traditionally, commercial organic MBs are made from lipid materials or liposomes for use as US imaging contrast agents, e.g., the lipid-coated perfluorocarbon (PFC) MB agent [10,11], and these MBs undergo an

* Corresponding authors.
E-mail addresses: youyin.chen@gmail.com (Y.-Y. Chen), sanyuanchen@mail.nctu.edu.tw (S.-Y. Chen).

0168-3659/$ – see front matter © 2013 Published by Elsevier B.V.
http://dx.doi.org/10.1016/j.jconrel.2013.07.029

instant phase transition into echogenic gas bubbles to intensify the US contrast through bubble-induced acoustic effects. However, these organic materials are usually soft and unstable because of their limited circulatory lifetime, which results from the easy dissolution of gas [12,13]. In contrast, a solid bubble shell can increase the stability of the contrast agent, such as silica [14,15], and can improve US contrast by increasing the backscattered signals. Liu et al. [16] reported a hydroxyapatite (HA)-coated liposome decorated with iron oxide nanoparticles that exhibited US-triggered drug release with MR imaging contrast but could not be used for US imaging because no gas was entrapped in the liposome. However, the enhancement in the contrast is still limited. Recent studies have reported that the presence of SPIO nanoparticles in the bubble shell can alter the surface tension of bubbles, can boost the acoustic impedance and can enhance the detectable backscatter [17]; all these effects result in intensified scattering signals and, consequently, improved US imaging. Liu et al. [18] proposed a process for synthesizing magnetic nano-in-micro imaging probes through emulsion polymerization to form poly(butylcyanoacrylate) MBs with the iron oxide nanoparticles in the bubble shell. Recently, Sun et al. [19] reported superparamagnetic PLGA-iron oxide microcapsules for dual-modality US/MR imaging and high-intensity focused US breast cancer ablation. However, when used in diagnostic US, the MBs easily become trapped in the blood pool and are limited to the vascular system after intravenous injection because of their micro-scale size; thus these MBs cannot be used for tumor-targeted therapy and imaging. The ideal US bubbles must be smaller than a certain size to retain the EPR effect and must also show good contrast enhancement in US imaging combination of US-triggered drug release and an active target function such as MT.

In this study, we propose a novel one-pot emulsion method for the synthesis of SPIO-containing nanobubble composites composed of temperature-sensitive Pluronic F127 and high-polarity polyacrylic acid (PAA) polymers as contrast agents for MR–US dual-modality imaging with the HIFU-triggered release of *Carmustine* (bischloroethylnitrosourea, BCNU) [20]. The use of thermal-responsive characteristics provides a surfactant-free, facile process for the formation of a nano-in-nanobubble species with an SPIO-embedded shell of adjustable thickness. The SPIO nanoparticles in the shell of the bubble not only stabilize the structure of the nanobubble but also enhance the US contrast by MT. Most importantly, the concentration of magnetic SPIO in the nanobubbles can be controlled to optimize the imaging contrast and the efficiency of the HIFU-triggered drug release. PAA and Pluronic (PEO–PPO–PEO, F127) triblock copolymers were used to form the nanobubbles in this study because PAA can act as a polymer binder and hydrogen bond to the PEO segments to stabilize the nanobubble structure (through the formation and stabilization of the interpolymer complexes) [21,22]. Moreover, temperature-sensitive Pluronic was used to synthesize the nanobubble because nano-in-nanobubble formulations with varying cavity sizes can be produced by controlling the synthesis temperature and the emulsion ratio of PAA to F127; the latter can exhibit a reversible and large-volume transition (1000-fold), as reported by Choi et al. [23] In particular, these nano-in-nanobubbles possess the following significant characteristics: (i) the SPIO-embedded nanobubbles have a biocompatible shell (the PEO hydrophilic segment), which ensures safety and prolonged *in vivo* circulation time for *in vivo* applications [24,25]; and (ii) the SPIO-embedded nanobubbles have a greater stability than soft-shell bubbles under the applied US, and this greater stability not only increases the strength of the structure but also enhances dual-modality contrast imaging. (iii) SPIO-embedded nanobubbles can trigger drug release by US and can function as an active target by MT. Detailed characterizations of the nanobubbles, *in vivo* MRI imaging, and drug release for tumor therapy from HIFU exposure, are presented below.

2. Materials and methods

2.1. Materials

SPIO nanoparticles were prepared under airless conditions from commercially available reagents [26], and the mean particle diameter for the SPIO nanoparticles was 4.8 nm. Absolute ethanol (99.5%), benzyl ether (99%), 1,2-hexadecanediol (97%), oleic acid (90%), oleylamine (>70%), dichloromethane (DCM) (99.9%), and iron (III) acetylacetonate were purchased from Sigma-Aldrich Co., St Louis, MO, USA. Perfluoropentane (PFP, C_5F_{12}) was purchased from ABCR GmbH & Co. KG (Karlsruhe, Germany). Nanobubbles with outer layers of polyacrylic acid (PAA) and Pluronic F127 were prepared through a single emulsion solvent evaporation (oil-in-water emulsion) process. PAA and Pluronic F127 were purchased from Sigma-Aldrich. *Carmustine* (BCNU, Sigma Chemical Co., St Louis, MO, USA), which is a DNA alkylating agent that is effective against glioma, was used as the model drug.

2.2. Preparation of BCNU-loaded nanobubbles

To prepare the BCNU@nanobubbles, 2 mL (14.1, 18.8, and 28.2 mg/mL) of SPIO nanoparticles was dispersed in 2 mL of DCM (5 mg BCNU/mL DCM) to form a uniform organic phase. A total of 100 mg of PAA, which was used as a polymer binder, was dissolved in 2 mL of deionized (DI) water at room temperature. A total of 160 mg of Pluronic F127, which was used as a temperature-sensitive factor, was dissolved in 8 mL of DI water. After the PAA and F127 were fully dissolved in the solution, both the polymer solutions (2 + 8 mL) were mixed to form an aqueous solution; then, the organic phase (2 mL) was added and the mixture was emulsified for 1 min with an ultrasonicator at 100 W. Next, the mixture was heated at 40 °C to moderately and gradually remove the organic phase over 2 h, and the solution volume clearly decreased. Subsequently, the mixture was heated to a higher temperature (55 °C) above the critical micelle temperature of the temperature-sensitive polymer to promote a stable nanoparticle. Next, a cooling process was applied to form a stable nanoparticle with hollow structure. In order to make a nanobubble filled with perfluoropentane (PFP) vapor [27], the hollow nanoparticles were frozen in a −80 °C freezer and lyophilized (FreeZone2.5, LABCONCO, USA) to fully dry the hollow nanoparticles. After lyophilization, vapor filling was performed by first evacuating the hollow nanoparticles for approximately 20 min; then, a gas syringe was used to inject the PFP vapor from the headspace above liquid PFP into the vessel that contained the hollow nanoparticles; PFP vapor was added to a pressure of 1 atm. When PFP was introduced, the PFP vapors were in contact with the hollow nanoparticles for 2 h and then degassed water was added to trap the PFP vapors inside the nanobubbles [28].

2.3. Measurement

The morphology of the nanobubbles was examined with transmission electron microscopy (TEM, JEOL Ltd, Japan, JEM-2100) and scanning electron microscopy (SEM, JEOL Ltd, Japan, 6700F). The particle sizes and distribution were analyzed by dynamic light scattering (DLS, Beckman Coulter, Inc., USA, Delsa™ Nano C, Particle Analyzer), which used a flow-through light scattering cell (0.7 mL) to determine the electrophoretic movement of charged particles under an applied electric field from the Doppler shift of scattered light. The particles were analyzed at different temperatures from 293 K to 333 K. In detail, we heated the sample (from 30 °C) at a rate of 1 °C/min, and measured the particle sizes at 30, 32, 35, 40, 45, 50, 55, and 60 °C. Before cooling the sample, we held the temperature at 60 °C for 5 min, and started to cool the sample at 1 °C/min and measured the particle sizes at 55, 50, 45, 40, 35, 30, 28, 25, and 20 °C. The magnetization of the nanoparticles was measured with a superconducting quantum interference device

(SQUID, Quantum Design, USA, MPMS-XL7) at 298 K and an applied magnetic field of ±10,000 G. Before the SQUID analysis, the iron oxide nanoparticles and nanobubbles were dried in a vacuum oven at 298 K for 48 h. To measure the relaxivity of the nanobubble, MR *in vitro* assays were performed with a 7 Tesla Bruker Biospec 70/30 USR MRI scanner (Bruker BioSpin MRI GmbH, Ettlingen, Germany; software: ParaVision 5.0). All samples were scanned in T2-weighted MRI scans with the MSME sequence (T_2/T_1 map; TR (ms) = 3000, 2000, 1000, 500, 300; TE (ms) = 11, 22, 33, 44, 55, 66, 77). The r_1 and r_2 were plotted as a function of the MNB concentration to respectively determine the r_2 relaxivities from the slopes of the linear fit. MR *in vivo* assays were performed with the same 7 T MR system. A 72 mm volume coil is used for transmission, and an actively decoupled single surface coil is used for signal reception (RAPID Biomedical GmbH, Rimpar, Germany). MR T_2 and T_2^* imaging (In gradient echo images, contrast depends on T_2^*, whereas in sequences with a 180° rephasing pulse, the contrast depends on T_2.) were performed with the TurboRARE sequence (TE =33 ms, TR = 2500 ms, TH = 1 mm, NEX = 4) and FLASH sequence (TE =335.1 ms, TR = 9.2 ms, TH = 1 mm, NEX = 2), respectively.

2.4. Phantom studies on US imaging and HIFU-triggered drug release in vitro

A SonoAce-X4 scanner (5 MHz) was used throughout this experiment (Medical It Supply Ltd., Korea). All of the operating parameters, including the focus point, gain, and depth, were constant for all of the imaging studies. All US imaging experiments were performed in a $4 \times 4 \times 4$ cm^3 agarose cubic phantom that had a hollow column 1 cm in diameter and 3 cm in depth in the middle of the cube. The concentration was maintained at 7 mg/mL, which is comparable to the concentration of commercial contrast agents that are injected *in vivo*. All parameters were maintained constant for all of the studies, and water was used to provide a standard control. The mechanical index (MI) was used to investigate the stability of the capsule against pressure.

The *in vitro* HIFU-triggered drug release from nanobubbles with various concentrations of iron oxide was evaluated by incubating the BCNU-containing nanobubbles in 20 mL of PBS. At specific time intervals, 1 mL of the medium was collected and was analyzed with a UV–visible spectrophotometer to determine the concentration of drug in the media (8453 UV–Visible Spectrophotometer, Agilent Technologies, Inc., USA); then, the volume of collected media was replaced with the same volume of fresh media. The measurements were performed in triplicate. A US focus transducer [29] was used throughout this experiment to trigger the release of the drug, and a slight amount of heat was generated (~2 °C), which is not enough to induce a temperature-sensitive polymer transition when the HIFU was employed. A spherical transducer (diameter, 60 mm; radius of curvature, 80 mm; frequency, 400 kHz, electric-to-acoustic efficiency, 70%; Imasonics Inc., Lyon, France) was used, and the center of the focal zone was positioned at a penetration depth of 2 to 3 mm in each hemisphere. A single burst of US was delivered with a duty cycle of 1% (10 ms on and 990 ms off), a pulse-repetition frequency of 1 Hz, and a total sonication duration of 300 s. For the optimization studies, the input electric power was 2 W, which corresponds to a negative acoustic peak. The amount of HIFU-induced release was determined by defining R_{ui}(i. e $R_{ui} = (M_{et} - M_{ct})$), where M_{et} and M_{ct} are the amounts of drug released from the experimental group and the negative control group, respectively, at time t.) The encapsulation efficiency (EE%) was determined by a comparison of the total release of BCNU into the solvent through HIFU treatment to the initial amounts of added drug. The EE% of BCNU was measured to be 92%, 52%, and 40% with respect to the SPIO-embedded concentrations of 14.1, 18.8, and 28.2 mg/mL, respectively, in the synthetic process.

2.5. US–MR tumor imaging and HIFU-triggered drug release in vivo

Female nude mice 24 weeks in age were purchased from the National Laboratory Animal Center (Taiwan). The rat glioma cell line RG2 (kindly provided by Dr. Tsung-Lang Chiou, Department of Neurosurgery, Tzu Chi General Hospital) was maintained in RPMI 1640 media supplemented with 10% fetal calf serum (FCS). For tumor implantation, all the mice were subcutaneously inoculated in the right hind leg with 10^4 to 10^5 cells resuspended in 100 μL of saline.

Fourteen days after cell implantation, 4 mice were used for the US–MRI dual-modality tumor imaging without any treatment. The animals were anesthetized through the administration of isoflurane (1.5 L/min oxygen in 2% isoflurane) with a facemask throughout the imaging process. US and MR imaging were performed with a clinical US scanner (SonoAce-X4, Medical It Supply Ltd., Korea) and a 7-Tesla MRI scanner (Bruker Biospin 70/30 USR, Billerica, MA), respectively. The US images were acquired with the contrast mode setting at a transmit frequency of 5 MHz and at 10% power. A catheter was placed in the tail vein to intravenously inject the 100-μL SPIO-embedded nanobubbles. After the nanobubbles were allowed to circulate for approximately 4 min, the transducer was positioned at the hind leg along the long axis of the tumor with a field of view of 40×40 mm^2 for 1 min. The acquired B-mode US images were used to qualitatively compare the enhancement of the signal before and after magnetic targeting (MT). For MR tumor imaging, the preparation steps and injection volume were the same as those used in the US imaging. The captured T_2-weighted images were used to qualitatively compare the enhancement in the contrast before and after MT.

To demonstrate the magneto-ultrasound therapy, the other mice ($n = 20$) were randomly divided into four therapeutic groups (5 mice/each group) seven days after the implantation with tumor cells. *Group 1* was a control group of CD1 nude mice in which 100 μL of saline was administered intravenously, starting on day 10 after the implantation of the tumor. *Group 2* was a treatment group of mice that, starting on day 7 after the implantation of the tumor, received an intravenous injection of 100 μL of SPIO-embedded BCNU@nanobubbles (*Carmustine*, 500 μg/mL) in combination with HIFU treatment in which the US beam was delivered to one location centered on the tumor site in the right leg. *Group 3* consisted of mice that were intravenously injected with 100 μL of SPIO-embedded BCNU@nanobubbles targeted to the tumor site with a focused magnetic field (1.18 T) for 5 min; this targeting caused a rapid accumulation of these nanobubbles. *Group 4* received intravenous injections of the SPIO-embedded BCNU@nanobubbles and was then subjected to MT for 5 min; following MT, HIFU was applied to the tumors on the mice injected with SPIO-embedded nanobubbles to trigger BCNU release. The sonication parameters described in Section 2.3 for the HIFU-triggered drug release were used with *Groups 3* and *4*. All experiments were approved by the Institutional Animal Care and Use Committee at the National Chiao Tung University and National Yang Ming University.

The size of the tumor was determined through the following formula: $(\mathbf{A} \times \mathbf{B}^2) / 2$, where **A** is the greater and **B** is the smaller measurement of the two dimensions [30]. The day when the mice began to be treated with the RG2 cells corresponded to day 0. The relative tumor volume was calculated as the volume at a given time divided by the volume on day 0 before the treatment began, and these values were expressed as percentages. The values are shown as the mean ± standard deviation [S.D.]. Statistical data analysis was performed with non-parametrical Wilcoxon–Mann–Whitney statistics. The mean relative tumor volumes for each treatment group were compared with those for the control group. $P < 0.05$ was considered to be statistically significant. The degree of variability and the range of values for the median were assessed in terms of 95% confidence intervals. The SPSS 2000, SYSTAT version 10 software package was used.

2.6. In-vivo biodistribution with/without MT

Healthy Wistar rats ($n = 48$) were subcutaneously inoculated with the rat glioma cell line RG2 in the right hind leg; 10^4 to 10^5 cells resuspended in 100 μL of saline were injected (inoculations were given for two weeks). The mice were divided into two equal groups. (Group I: nanobubbles only and Group II: nanobubbles combined with MT) and were intravenously injected (12 mg/kg, 300 μL) through the tail vein, respectively. Four rats per group were sacrificed and the organs (spleen, liver, kidney, heart, lung, brain tumor) were removed at circulation times of 30 min, 3 h, 6 h, 12 h, 24 h and 48 h following the administration of nanobubbles. Quantitative measurement of the iron concentration in the samples was determined by Inductively Coupled Plasma Optical Emission Spectrometry (ICP-OES, Perkin-Elmer OPTIMA-2000) after digestion with HCl/$KMnO_4$.

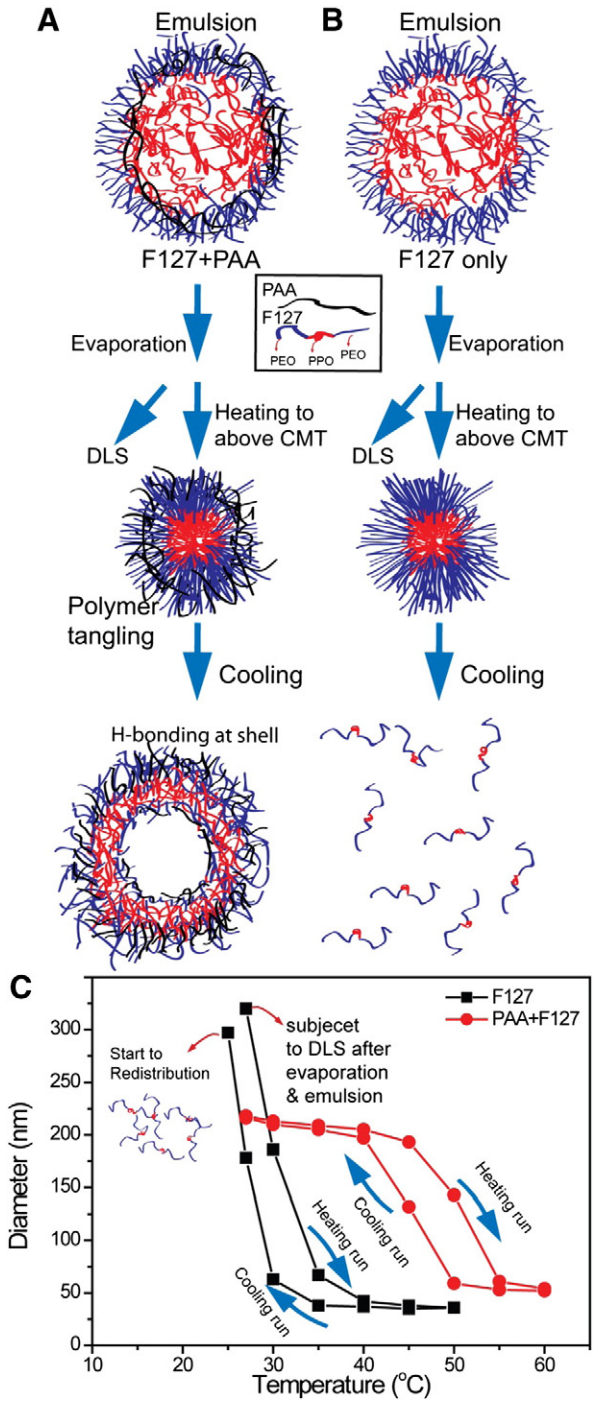

Fig. 1. (A) Showing the emulsion process can promote the formation of oil-in-water F127-based particles which would undergo the shrinkage at heating above the CMT and then the F127 was redispersed into water after cooling run. (B) The PAA was added to the system so that the hollow structure would retain its shape at lower temperatures and would not redistribute into the solution. (C) Illustrates that the pure F127 (2 wt.%) exhibited a redistribution state after the heating and cooling process. In the lower temperature region, no diameter can be detected, and this lack of detection results from the redistribution of F127 to the solution. In the PAA(1 wt.%) + F127(1 wt.%) system, there was a reversible loop in the heating and cooling process.

3. Results and discussion

3.1. Interpolymer hydrogen-bonding complexes

Pluronics are temperature-sensitive polymers composed of poly(ethylene oxide)–poly(propylene oxide)–poly(ethylene oxide). The delicate balance between hydrophilicity and hydrophobicity in the polymer structure was responsible for the phenomenon of the critical micelle temperature (CMT), at which a transition in aqueous solution was demonstrated, as shown in Fig. 1A. Generally, F127 undergoes a reversible process (without emulsifying) in the temperature cycles, and this reversible transition between micelle (~10 nm) and unimers was also well-known. In our case, since DCM was incorporated to the F127 solution to form emulsion state, the formation of oil-in-water F127-based nanoparticles (>100 nm) would be promoted. Subsequently, the particle would undergo shrinkage at heating above the CMT and then the F127 was redispersed into water after cooling run. However, it was noted that the transition between nanoparticle and unimers was an irreversible process. However, as the high-polarity polymer PAA was added, a stable hollow structure was formed, as shown in Fig. 1B, because of the formation and stabilization of interpolymer hydrogen-bonding complexes (IPHBCs) between the PAA and F127 (PEO_m–PPO_n–PEO_m) in solution after cooling. These IPHBCs arose because of the cooperative and hydrophobic effects, which depend on various internal–external parameters [22,31]. Such complexation can induce the formation of a stable core–shell structure in which the tangled PPO comprises the core and the remaining soluble block of PEO complexed with PAA forms the shell. The SEM images corresponding to Fig. 1A and B are showed in Fig. S1a and S1b, respectively where a polymer film-like was observed in Fig. S1a but a hollow structure appeared in Fig. S1b. When the temperature was less than 25 °C, the PPO segment changed from nonpolar to polar (soluble), and the segment was redistributed into the solution. The change in the particle diameter as a function of temperature from heating to cooling is illustrated in Fig. 1C; the PPO block in the F127 (PEO–PPO–PEO) (2 wt.%) solution began to shrink as the temperature rose and thus formed a particle structure. The particle size substantially decreased from ~310 nm to ~50 nm with a further increase in the temperature because the hydrophobicity in the PPO blocks of F127 strongly varies with temperature. During the cooling run, the transition state occurred at 28 °C, and the particle reached a maximum size and then rapidly redistributed into the solution state. In contrast, when 1 wt.% PAA was added to the F127 solution to form an emulsion, the PPO segment gradually became nonpolar as the solution temperature increased, and the PPO segment started to aggregate in the high polarity environment (adding PAA). Furthermore, it was observed that PAA prevented the redistribution of F127 during cooling from 60 °C to room temperature because of hydrogen bonding. Most importantly, the expansion in volume of the preformed nanoparticles led to the formation of a stable, hollow nanocapsule during the cooling cycle. The pyrene excitation spectra were further to prove the results. The change of slope in the I_1/I_3 ratio (Fig. S2a) in cooling run indicated that the F127 particle dissolved into solution releasing pyrene into solution, and no particle size distribution can be measured by DLS. On the other hand, the same slope in Fig. S2b indicated the F127 + PAA particle remained and exist without redistributing into solution.

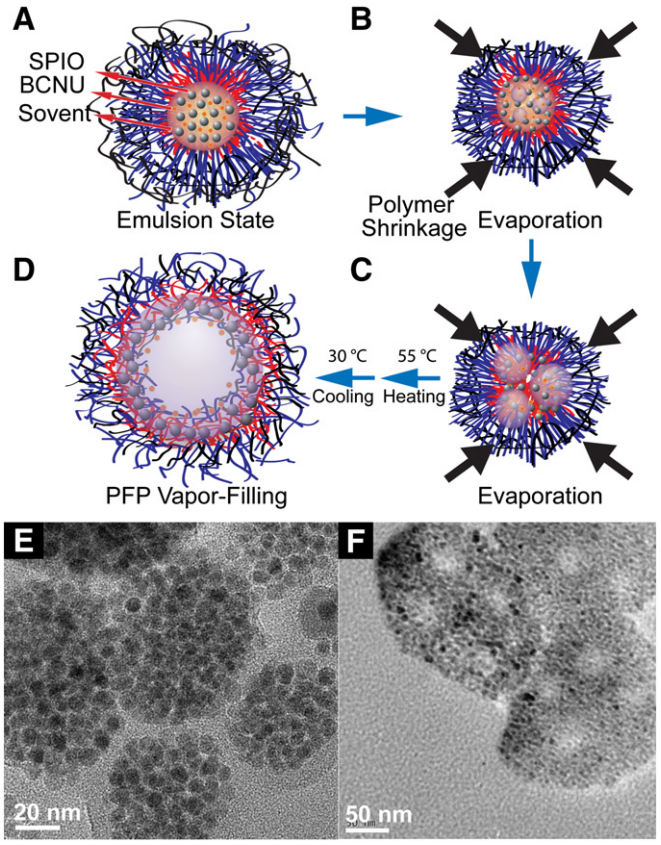

Fig. 2. Detailed mechanism for the formation of SPIO-embedded nanobubbles. (A) shows that the emulsion nanoparticle is composed of dense SPIO in the particle core with a polymer shell. (B) and (C) are the evaporation stage of the emulsion nanoparticles that may induce the pores formed in the particle. (D) shows that after cooling and filling with vapor, stable hollow structures were formed. The TEM images in (E) and (F) are corresponding to the (A) and (C), respectively.

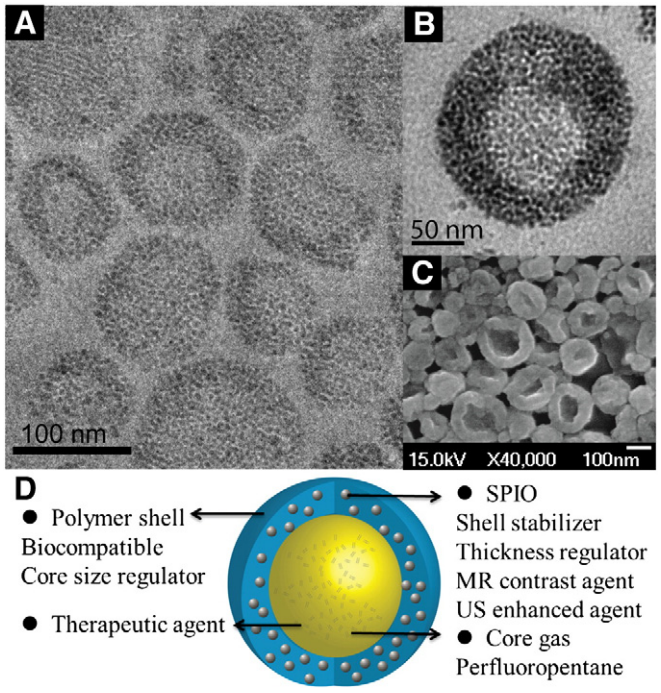

Fig. 3. (A) and (B) TEM images at different magnifications. (C) SEM images that show the collapsed bubbles under vacuum. (D) Detailed features of the nanobubble produced through the one-step emulsion process; the SPIO played an important role in this system.

3.2. Characterization of the nanobubble synthetic process

Fig. 2 schematically illustrates the fabrication of a nanobubble with hollow structure through a surfactant-free one-step emulsifying process using F127–PAA and superparamagnetic iron oxide (SPIO) nanoparticles. When the aqueous phase (deionized water) with dissolved PAA and F127 was mixed with an organic solvent (DCM) that contained hydrophobic SPIO nanoparticles (~5 nm) and hydrophobic drug BCNU, an oil-in-water (O/W) emulsion formed in which the SPIO nanoparticles were localized in the core of the PAA–F127 nanoparticles. To successfully perform the nanobubble fabrication process, both concentrations of PAA and the SPIO content are crucial. The hydrogen bonding between PAA and PEO (one block of F127) in the shell can stabilize the structure of the nanobubble. The initial oil-in-water emulsion state (Fig. 2A) was acquired during the synthetic process and the corresponding TEM image was shown in Fig. 2E. As the temperature was increased to 40 °C (Fig. 2B), the DCM (boiling point = 38 °C) gradually evaporated from the core of the nanoparticles. After evaporation, the TEM image showed that few pores appeared in the core (Fig. 2F). However, once the temperature increased to 55 °C, the particle structure became more stable by surpassing the CMT of F127 + PAA (tangling each other). After the cooling process, the thermal sensitive polymer of F127 would expand, and the SPIO nanoparticles were partially attracted to the shell because of the affinity of SPIO to the hydrophobic PPO segments of F127. Subsequently, a stable hollow structure with the hydrophobic SPIO nanoparticles in the shell formed during the cooling process. Next, PFP vapor filling was applied, and the nanobubbles exhibited a hollow structure as shown in Fig. 2D.

3.3. Characterization and morphology of the nanobubbles

To observe the morphologies of the nanobubbles, the dried samples were examined with scanning electron microscopy (SEM) and transmission electron microscopy (TEM). As expected, the TEM image of the nanobubbles in Fig. 3B exhibits a hollow structure surrounded by SPIO in the shell, and the thickness of the shell was estimated to be approximately 20–50 nm. The TEM image in Fig. 3B reveals brighter contrast in the center of the nanobubbles because the electron beam is scattered by less material. The SEM image in Fig. 3C reveals a concave morphology and a "bowl-like" appearance, which was caused by the collapse of the nanobubbles under vacuum. The configurations of the nanobubbles can be understood through the following balloon analogy: a wet nanobubble is similar to a gas-filled balloon, and after drying, the nanobubble collapses similarly to the way a deflated balloon collapses. However, the nanobubble is reinforced by SPIO, so the nanobubble is relatively rigid and is capable of supporting a bowl shape or a buckled bowl shape. Furthermore, the particle size distribution after 30 days was comparable to the original distribution, this result indicates that the nanobubble is very stable. Conversely, conventional ultrasound microbubble imaging agents with soft shells, such as albumin or lecithin, have been shown to persist for only 15–20 min in tissues. Fig. 3D summarizes the advantages of SPIO-embedded nano-in-nanobubbles, including the role of SPIO as a structure stabilizer, shell thickness regulator, MR contrast agent, magnetic guiding probe, and US contrast enhancer.

Furthermore, while modifying the concentration of SPIO, it was observed that for a fixed polymer weight ratio of PAA/F127 (for example, 2/3) and an SPIO concentration below 9.4 mg/mL, nanobubbles were unable to form (were unstable). However, at a concentration greater than 9.4 mg/mL, stable nanobubbles could be synthesized easily and

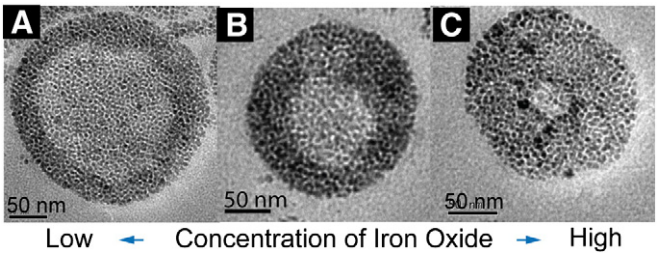

Fig. 4. (A–C) TEM images of nanobubbles with SPIO concentrations of 14.1, 18.8, and 28.2 mg per mL in the synthetic process. As shown, the thickness of the shell varied with the SPIO concentration. This result implies that increasing the SPIO concentration leads to an increased shell thickness.

could be preserved with long-term stability (several months), during which time the size and monodispersity of the nanobubbles did not change. This result indicates that SPIO plays an important role in stabilizing the nanobubbles. In addition, the size of the nanobubbles only slightly decreased as the SPIO concentration increased, as shown in Fig. 4A–C; the size range was 215–230 nm for an SPIO concentration of 14.1 mg/mL and was 180–205 nm for a concentration of 28.2 mg/mL; these results are very consistent with the dynamic light scattering measurements, as shown in Fig. S3. However, the thickness of the shell of the nanobubble increased as the SPIO concentration increased; this increased thickness indicates that the core size will be smaller as the concentration of SPIO increases.

3.4. Ultrasonic contrast as a function of polymer ratio and SPIO concentration

As mentioned above, the CMT and volume change of the nanobubbles can be varied through chemical modification of the PAA/F127 ratio, modification of this ratio enables these polymers to be tailored for diverse contrast enhancements and for drug-release applications. Increasing the PAA concentration results in stronger interactions and less volume shrinkage because PAA introduces more hydrophilic functional groups into the nanostructures. In contrast, at a PAA/F127 ratio of less than 1/4, the nanoparticle becomes unstable because of the incompact loose structure at room temperature. Therefore, the nanoparticles with PAA/F127 ratios from 4:1 to 2:3 remained stable and exhibited considerable volume shrinkage.

The ultrasonic sensitivity of the nanobubbles depends on the relative composition ratio of PAA to F127, as shown in Fig. 5A, in which the ultrasonic enhancement of the degassed and deionized water is nearly zero (Fig. 5B). As more F127 polymer was used, the contrast enhancement was increased because the F127 is capable of withstanding substantial volume changes due to its flexible and biocompatible character. Thus, an increased volume change occurs in the nanobubbles during the synthetic process, and the inner hollow core is larger when greater amounts of F127 are used. This hollow inner core occurs through inertial cavitation (IC) when the nanobubbles are subjected to acoustic pressure [32]. The highest average gray value of 62 appeared at a PAA/F127 ratio of 2/3; however, a lower average gray value of 35 occurred at a PAA/F127 ratio of 1/4 because a higher F127 fraction leads to an unstable structure (which is easily disrupted under US) that is easily redissolved in water (not enough interpolymer hydrogen-bonding complexes). When the SPIO was introduced into the nanobubbles at a PAA/F127 ratio of 2/3, the US contrast imaging in the SPIO-embedded nanobubbles was significantly enhanced. Compared to the nanobubbles that did not contain embedded SPIO, the enhancement was distinctly increased 2-fold (from a mean gray scale value of 62 to 115), after the embedding of SPIO into the nanobubbles in the PAA-F127 system at an SPIO concentration of 18.8 mg/mL; a brighter image was clearly observed at this concentration (Fig. 5E). The SPIO-embedded nanobubbles were not only resonant with the US but also backscattered the US signal. After the embedded concentration surpassed 28.2 mg/mL, the cavity size of the nanobubble decreased, and because the cavity was too small to create inertial cavitation with the US, the nanobubble contrast efficiency decreased.

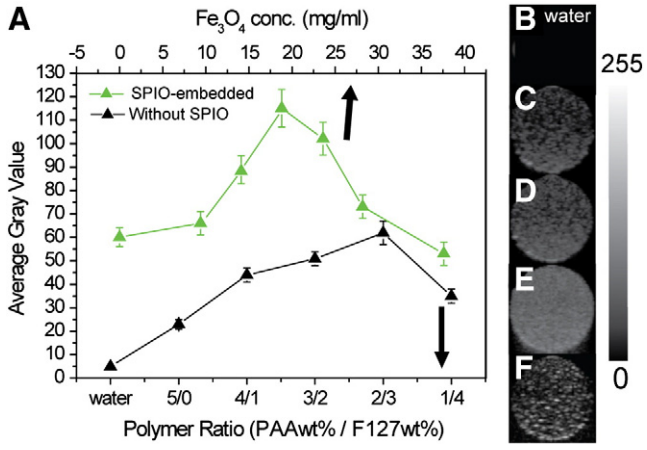

Fig. 5. (A) US contrast enhancement for different polymer ratios; there was a 2-fold enhancement in contrast when the SPIO was added. (B) The degassed and deionized water ultrasonic contrast. (C)–(F) *In vitro* images of the nanobubbles with US contrast at embedded SPIO concentrations of 9.4, 14.1, 18.8, and 28.2 mg/mL.

3.5. MR contrast as a function of SPIO concentration

The SPIO-embedded nanobubbles appear to be suitable candidates for T_2-type MRI contrast enhancement agents because of the high saturation magnetization and low cytotoxicity of the nanobubbles. Fig. S6 presents the inverse relaxation times, $1/T_2$, as a function of the molar concentration of Fe. The inverse relaxation times varied linearly with the Fe concentration, and the slope was defined as the transverse (r_2) relaxivity. The efficacy and stability of the nanobubbles as an MR contrast agent was further evaluated by measuring the longitudinal (r_1) and transverse (r_2) relaxivities with an MR scanner. The lower longitudinal relaxivity of r_2 could result from the encapsulated SPIO nanoparticles that were embedded in the hydrophobic PPO blocks of F127; these blocks reduced the close contact between the water molecules and the magnetic nanoparticles. Meanwhile, r_2 values of 208, 183, and 164 (s^{-1} mM^{-1} Fe) were measured at embedded SPIO concentrations of 28.2, 18.8 and 14.1 (mg/mL), respectively. Similar results were obtained when the nanobubble dispersions were maintained in the magnetic field for 17 h. This stability can be attributed to the presence of free PEO chains on the surface of the nanobubbles; these chains effectively reduce dipole–dipole attractions among the nanobubbles and prevent aggregation under high magnetic fields. Therefore, the developed SPIO-embedded nanobubbles could perform well as T_2-type MR contrast enhancement agents in cell or tissue imaging and in diagnostic applications. Fig. S6c–e presents the T_2-weighted MR images of aqueous dispersions of SPIO-embedded nanobubbles with different concentrations of embedded SPIO. As shown, the MR contrast increased as the quantity of nanobubbles increased; this result demonstrates that the efficiency of the magnetic nanoparticles in the nanobubbles enhanced the transverse (T_2) proton relaxation process.

3.6. In vitro evaluation of drug release with exposure to HIFU

The ultrasonically triggered drug release behavior of drug-loaded SPIO-embedded nanobubbles (with a PAA/F127 ratio of 2/3) was evaluated under exposure to HIFU for 300 s. The drug release profiles of the SPIO-embedded nanobubbles were recorded as functions of the SPIO thickness and the HIFU treatment time. The SPIO-embedded nanobubbles demonstrated significant HIFU-induced release behavior,

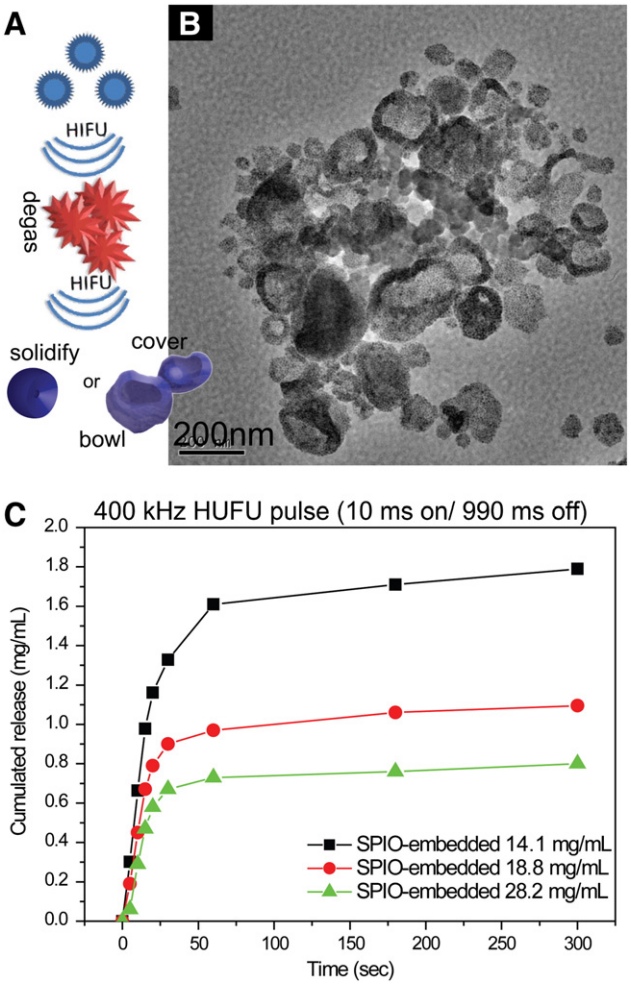

Fig. 6. (A) Diagram that illustrates the reaction of the nanobubble with HIFU. After HIFU exposure; (B) the TEM image of the collapsed cavitation fragment structures of cover-bowl and solidified nanobubbles after the application of HIFU. (C) The drug release behavior under HIFU with a frequency of 400 kHz and pulsed US with a duty cycle of 1% (10 ms on 990 ms off) for different concentrations of embedded SPIO.

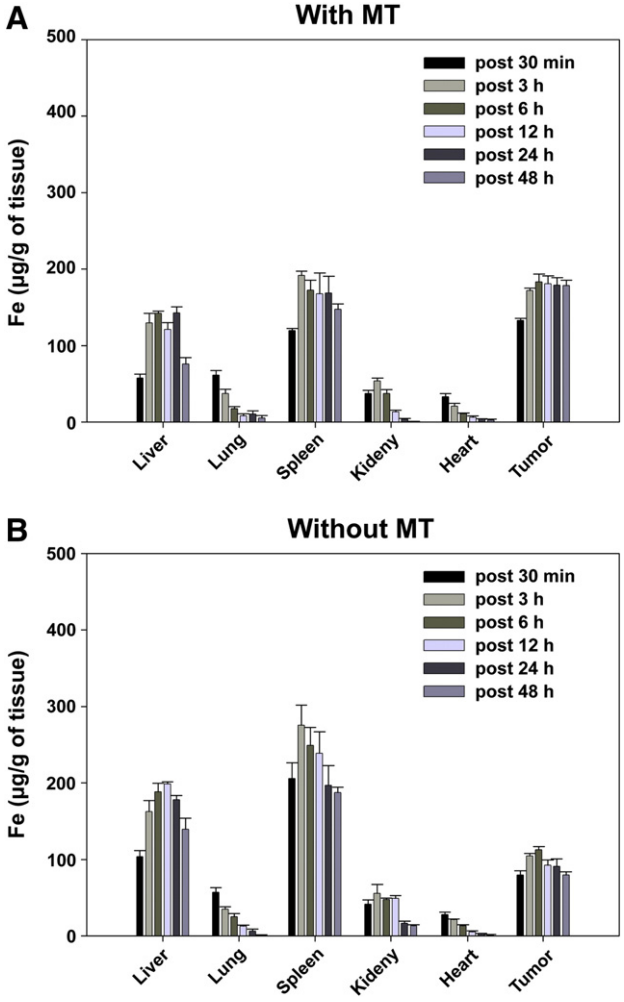

Fig. 7. (A) Biodistribution of nanobubbles obtained 30 min to 48 h after administration in rats with (A) magnetic treatment (MT) and (B) without magnetic treatment. The results are expressed as injected dose per gram of tissue from the inductively coupled plasma (ICP) study of iron ions.

as shown in Fig. 6A. As explained in the basic theory of US, the maximum amplitude of the pressure pulse induced by HIFU can be illustrated by MI. This amplitude is calculated as the peak negative pressure (P, which is proportional to the square root of the US power density) divided by the square root of the US frequency. Consequently, at a constant pressure pulse amplitude (image scanner), a high frequency (3–5 MHz) was observed; this result implies that low MI is not sufficiently large to collapse the structure of the nanobubbles. However, at a similar pressure pulse amplitude, a low frequency (400 kHz) might easily collapse the "nanocomposite" SPIO-embedded nanobubble and cause a prominent HIFU-induced drug release. As illustrated in Fig. 6A, the HIFU altered the morphology of the nanobubbles so that the nanobubbles collapsed (solidification) or assumed a fragmented structure (cover-bowl structure). This reaction was demonstrated by TEM photographs (Fig. 6B) of the SPIO-embedded nanobubbles after exposure to HIFU; these images demonstrate that the SPIO-embedded nanobubbles collapsed after exposure to HIFU. The cumulative released drug concentration was estimated to be 1.79, 1.09 and 0.8 mg/mL in 300 s for the nanobubbles with SPIO-embedded concentrations of 14.1, 18.8, and 28.2 mg/mL, respectively (Fig. 6C). As the SPIO-embedded nanobubbles were exposed to HIFU, it was found that the SPIO-embedded nanobubbles collapsed and the loaded drug was completely released from the nanobubbles. The cumulative percentage of drug released from the nanobubbles was calculated to be approximately 95% based on the EE% after exposure to HIFU, indicating that the entire loaded drug was almost released from the nanobubbles.

3.7. In vivo biodistribution with and without MT

To evaluate how the MT affects the biological behavior of nanobubbles in the living animals, nanobubbles with and without MT were used for the biodistribution study in tumor rats (Fig. 7). As expected, the nanobubbles showed high accumulation and long retention in the liver and spleen and then slowly decreased over the next 2 days relative to the other organs (kidney, heart, lung, and tumor). Meanwhile, the iron uptake in the other organs was slightly but not significantly higher with time. The biodistribution studies in tumor rats indicated that the MT of the nanocarriers affects the distribution. In Fig. 7A, the nanobubbles with MT showed a desirable tissue distribution profile (much more tumor uptake and retention).

3.8. Therapeutic efficacy

In vivo US imaging experiments were performed as proof of principle experiments [18]; therefore, we selected the nanobubbles with the greatest ultrasonic contrast (a PAA/F127 ratio of 2/3, and an SPIO-embedded concentration of 18.8 mg/mL) to achieve the best contrast efficacy during the experiments. In the contrast-enhanced US

experiment presented in Fig. 8A–B, significant image contrast can be observed in the middle areas of a rat glioma tumor (inoculated in the right hind leg) upon the injection of SPIO-embedded nanobubbles into the tail vein (Fig. 8A). A magnet (1 cm in diameter, 2 mm in thickness, 1.18 T) was positioned over the tumor for 30 s as a magnetic guide, and an enhanced acoustic image clearly revealed a 2-fold increase in the ultrasonic signal intensity in the ventral side of the tumor after 30 s of MT (Fig. 8B).

As mentioned above, the nanobubble shell provided a high saturation magnetization of 57 emu/g Fe (Fig. S6), which suggests that the nanobubble can be captured within a tumor mass by applying MT. Moreover, the high T_2 relaxivity of 183 (s^{-1} mM^{-1} Fe) indicated a possibility for noninvasive monitoring of nanobubble delivery to the target site by *in vivo* T_2 MRI. The contrast-enhanced MR images were acquired before administration of the SPIO-embedded nanobubbles, and at 2 h post injection, an external magnet was fixed to the tumor for 30 s. There was significant accumulation and retention of the SPIO-embedded nanobubbles in the contrast-enhanced region (tumor blood vessels), as shown in Fig. 8D, in which the signal intensity of the T_2-weighted MRI of the nanobubbles was approximately 1.5-fold less than the same region without MT targeting, as shown in Fig. 8C. These animal experiments demonstrated that the developed SPIO-embedded nanobubbles exhibited acceptable US–MRI image contrast capabilities *in vivo* and that the nanobubbles can consequently be considered for *in vivo* magnetic guidance and for therapeutic delivery with HIFU exposure (dual targeting treatments). Here, a custom-built HIFU system [33] was used for our study, and the system configuration consisted of a fixed, focusing HIFU head and an US control unit. An anesthetized animal was fixed in a reclining position on the stage, and a rubber film was used to seal degassed water between the HIFU transducer and the skin to locate the target region on the hind leg (Fig. 8E).

According to the tumor growth curve in the preliminary study shown in Fig. 8F, the tumors in *Group 2*, with injection of BCNU@nanobubbles and HIFU exposure, exhibited half the growth rate of the tumors in *Group 1*, which had a saline injection ($P < 0.05$). In this study, HIFU exposures were conducted in the tumor region at 1% duty cycles in which nonthermal mechanisms, such as acoustic cavitation and radiation forces, predominate [34,35]. The relatively short duty cycle of the HIFU exposure has been shown to increase the delivery and consequent therapeutic effects of the drugs [35,36]. The tumors in *Group 4*, with injection of BCNU@nanobubbles and MT, showed significantly reduced growth compared to the tumors in *Group 1*, which had a saline injection ($P < 0.05$). This result suggests that magnet-mediated targeting could result in an increased concentration of BCNU@nanobubbles in tumors and could reduce the circulating levels of the anticancer drug complex and thus reduce the toxic effects of the drug [37–39].

The MT of the BCNU@nanobubbles with HIFU exposure in *Group 3* manifested the slowest tumor growth rate relative to *Group 1* with saline injection ($P < 0.01$) and the other treatment groups ($P < 0.05$). Enhanced accumulation of the SPIO-embedded nanobubbles in the tumor tissue can be achieved with MT. However, this enhanced accumulation does not guarantee successful therapy if the anticancer drug does not reach the target site of the tumor cell, such as the cell membrane, cytosol, or nucleus [40,41]. In this study, the HIFU delivery technology enabled the release of high concentrations of anticancer drug from nanobubbles that were preferentially deposited in the tumor tissue, and the HIFU temporarily increased the permeability of the tumor cell membranes and promoted transmembrane uptake of the released anticancer drug

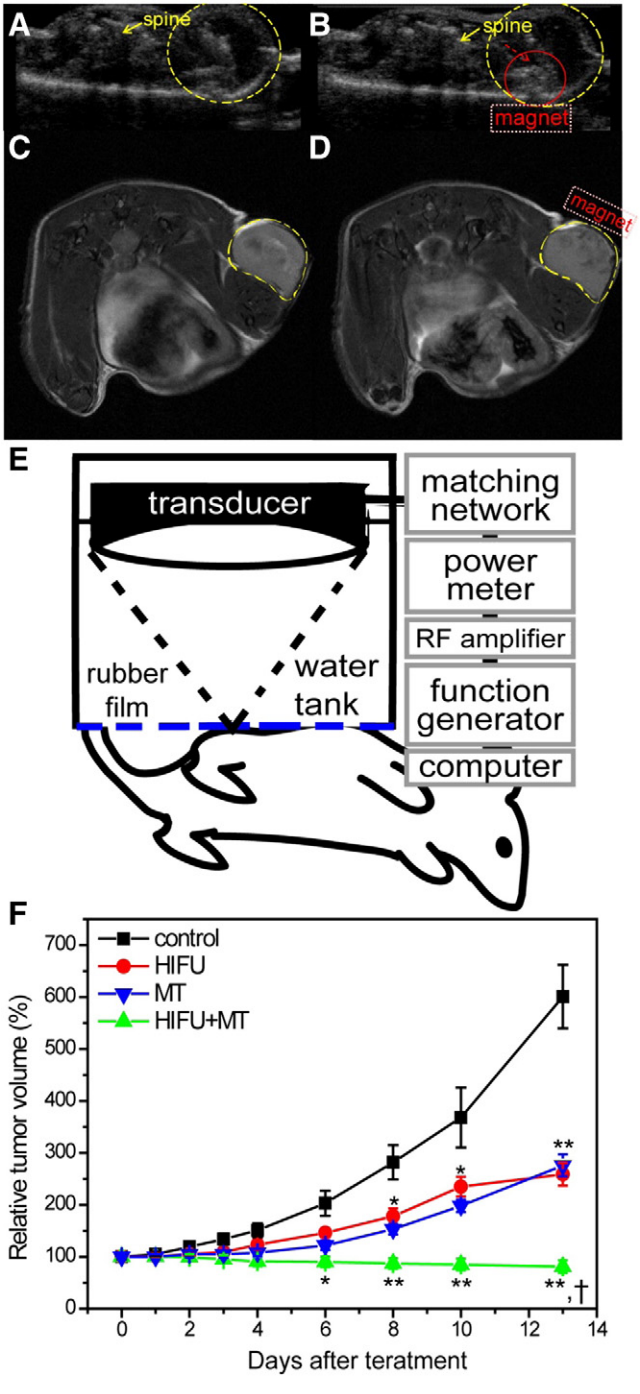

Fig. 8. (A) Transverse US image obtained from a mouse with a subcutaneously implanted glioma tumor (yellow dotted circle) following the intravenous injection of SPIO-embedded nanobubbles. Contrast enhancement was observed between the solid tumor and the surrounding healthy tissues in the US image. Compared with (A) before the MT treatment, (B) additional contrast enhancement appeared in the ventral region (red arrow) when a magnet was attached over the tumor area with surgical tape. (C) Coronal T_2-weighted images obtained in a mouse with a subcutaneously implanted tumor following the intravenous injection of SPIO-embedded nanobubbles. After 30 s of MT, the magnet was removed before imaging. (D) The magnetically targeted tumor (right, yellow solid circle) appears darker than before MT, and this darkness indicates the preferential accumulation of SPIO-embedded nanobubbles through MT. (E) Schematic diagram of the *in vivo* HIFU system. The system was composed of an HIFU transducer mounted horizontally inside a water tank filled with degassed water and a HIFU control unit (a computer-controlled system for HIFU-exposure sequences). A focused US beam was applied with the computer-controlled system and was then coupled to the tumor through a water tank. (F) Analysis of tumor growth (relative to day 0) as a function of time post-treatment for the untreated control tumors ($n = 4$, *Group 1*), tumor treatments with only HIFU exposure ($n = 4$, *Group 2*), with MT and HIFU exposures ($n = 4$, *Group 3*) and with only MT exposure ($n = 4$, *Group 4*). The results were expressed as the mean ± SD for each group. *Significantly different from *Group 1* at the same time point ($P < 0.05$). **Significantly different from *Group 1* at the same time point ($P < 0.01$). †Significantly different from *Group 2* or *Group 4* at the same time point ($P < 0.05$).

into the cytoplasm of the tumor cells [42]. In summary, the combined MT and HIFU strategy enabled the developed nanobubbles to enhance both the passive targeting and active targeting of potentially useful chemotherapeutic drugs to tumors.

4. Conclusions

In this study, we synthesized PFP-encapsulated PAA–F127 thermosensitive nanobubbles with shell thicknesses of 20–50 nm, and ~5 nm SPIO Fe_3O_4 superparamagnetic nanoparticles were loaded in the shells to significantly enhance the ultrasonic contrast and the magnetic susceptibility. The *in vivo* MR susceptibility experiments demonstrated that the SPIO-embedded nanobubbles can be magnetically guided to the target site (tumor) to locally enhance the contrast in US and MR imaging. Furthermore, by combining MT with HIFU, the nanobubbles enhanced the passive targeting and physical targeting of tumors and the HIFU-triggered drug release for tumor therapy. Future research on nanobubbles will focus on the treatment of brain tumors, especially the opening of the blood–brain barrier, and nanobubbles will be investigated as potential vehicles for image-guided, magnetically targeted and US-mediated drug delivery.

Acknowledgments

This work was financially supported by the National Science Council of the Republic of China, Taiwan under the contract NSC100-2320-B-009-006-MY2. This work is also supported by "Aim for the Top University" program of the National Chiao Tung University and Ministry of Education, Taiwan, ROC. We also thank the 7T animal MRI Core Lab of the Neurobiology and Cognitive Science Center for technical and facility support, and C. H. Hsieh and J. H. Chen of the Instrumentation Center at National Taiwan University for the MRI experiments.

Appendix A. Supplementary data

Supplementary data to this article can be found online at http://dx.doi.org/10.1016/j.jconrel.2013.07.029.

References

[1] A.L. Klibanov, T.I. Shevchenko, B.I. Raju, R. Seip, C.T. Chin, Ultrasound-triggered release of materials entrapped in microbubble-liposome constructs: a tool for targeted drug delivery, J. Control. Release 148 (2010) 13–17.
[2] F. Yan, L. Li, Z. Deng, Q. Jin, J. Chen, W. Yang, C.-K. Yeh, J. Wu, R. Shandas, X. Liu, H. Zheng, Paclitaxel–liposome–microbubble complexes as ultrasound-triggered therapeutic drug delivery carriers, J. Control. Release 166 (2013) 246–255.
[3] A. Raisinghani, A.N. DeMaria, Physical principles of microbubble ultrasound contrast agents, Am. J. Cardiol. 90 (2002) 3–7.
[4] J.-M. Correas, L. Bridal, A. Lesavre, A. Méjean, M. Claudon, O. Hélénon, Ultrasound contrast agents: properties, principles of action, tolerance, and artifacts, Eur. Radiol. 11 (2001) 1316–1328.
[5] V. Sanna, G. Pintus, P. Bandiera, R. Anedda, S. Punzoni, B. Sanna, V. Migaleddu, S. Uzzau, M. Sechi, Development of polymeric microbubbles targeted to prostate-specific membrane antigen as prototype of novel ultrasound contrast agents, Mol. Pharm. 8 (2011) 748–757.
[6] J. Wu, H. Leong-Poi, J. Bin, L. Yang, Y. Liao, Y. Liu, J. Cai, J. Xie, Y. Liu, Efficacy of contrast-enhanced us and magnetic microbubbles targeted to vascular cell adhesion molecule-1 for molecular imaging of atherosclerosis, Radiology 260 (2011) 463–471.
[7] T. Yin, P. Wang, R. Zheng, B. Zheng, D. Cheng, X. Zhang, X. Shuai, Nanobubbles for enhanced ultrasound imaging of tumors, Int. J. Nanomedicine 7 (2012) 895–904.
[8] Y. Chen, Y. Gao, H. Chen, D. Zeng, Y. Li, Y. Zheng, F. Li, X. Ji, X. Wang, F. Chen, Q. He, L. Zhang, J. Shi, Engineering inorganic nanoemulsions/nanoliposomes by fluoride–silica chemistry for efficient delivery/co-delivery of hydrophobic agents, Adv. Funct. Mater. 22 (2012) 1586–1597.
[9] Y. Chen, Q. Yin, X. Ji, S. Zhang, H. Chen, Y. Zheng, Y. Sun, H. Qu, Z. Wang, Y. Li, X. Wang, K. Zhang, L. Zhang, J. Shi, Manganese oxide-based multifunctionalized mesoporous silica nanoparticles for pH-responsive MRI, ultrasonography and circumvention of MDR in cancer cells, Biomaterials 33 (2012) 7126–7137.
[10] R. Suzuki, Y. Oda, N. Utoguchi, K. Maruyama, Progress in the development of ultrasound-mediated gene delivery systems utilizing nano- and microbubbles, J. Control. Release 149 (2011) 36–41.
[11] . B. Geers, H. Dewitte, S.C. De Smedt, I. Lentacker, Crucial factors and emerging concepts in ultrasound-triggered drug delivery, J. Control. Release 164 (2012) 248–255.
[12] K.W. Ferrara, Driving delivery vehicles with ultrasound, Adv. Drug Deliv. Rev. 60 (2008) 1097–1102.
[13] G.M. Lanza, S.A. Wickline, Targeted ultrasonic contrast agents for molecular imaging and therapy, Prog. Cardiovasc. Dis. 44 (2001) 13–31.
[14] P.-L. Lin, R.J. Eckersley, E.A.H. Hall, Ultrabubble: a laminated ultrasound contrast agent with narrow size range, Adv. Mater. 21 (2009) 3949–3952.
[15] X. Wang, H. Chen, Y. Chen, M. Ma, K. Zhang, F. Li, Y. Zheng, D. Zeng, Q. Wang, J. Shi, Perfluorohexane-encapsulated mesoporous silica nanocapsules as enhancement agents for highly efficient High Intensity Focused Ultrasound (HIFU), Adv. Mater. 24 (2012) 785–791.
[16] T.-Y. Liu, T.C. Huang, A novel drug vehicle capable of ultrasound-triggered release with MRI functions, Acta Biomater. 7 (2011) 3927–3934.
[17] F. Yang, Y. Li, Z. Chen, Y. Zhang, J. Wu, N. Gu, Superparamagnetic iron oxide nanoparticle-embedded encapsulated microbubbles as dual contrast agents of magnetic resonance and ultrasound imaging, Biomaterials 30 (2009) 3882–3890.
[18] Z. Liu, T. Lammers, J. Ehling, S. Fokong, J. Bornemann, F. Kiessling, J. Gätjens, Iron oxide nanoparticle-containing microbubble composites as contrast agents for MR and ultrasound dual-modality imaging, Biomaterials 32 (2011) 6155–6163.
[19] Y. Sun, Y. Zheng, H. Ran, Y. Zhou, H. Shen, Y. Chen, H. Chen, T.M. Krupka, A. Li, P. Li, Z. Wang, Z. Wang, Superparamagnetic PLGA-iron oxide microcapsules for dual-modality US/MR imaging and high intensity focused US breast cancer ablation, Biomaterials 33 (2012) 5854–5864.
[20] M.G. Ewend, S. Brem, M. Gilbert, R. Goodkin, P.L. Penar, M. Varia, S. Cush, L.A. Carey, Treatment of single brain metastasis with resection, intracavity carmustine polymer wafers, and radiation therapy is safe and provides excellent local control, Clin. Cancer Res. 13 (2007) 3637–3641.
[21] H.-Y. Huang, S.-H. Hu, C.-S. Chian, S.-Y. Chen, H.-Y. Lai, Y.-Y. Chen, Self-assembling PVA-F127 thermosensitive nanocarriers with highly sensitive magnetically-triggered drug release for epilepsy therapy *in vivo*, J. Mater. Chem. 22 (2012) 8566–8573.
[22] A. Beshee, J.r. Vogel, D. Glanz, J.r. Kressler, T. Groth, K. Mäder, Characterization of PLGA Nanospheres stabilized with amphiphilic polymers: hydrophobically modified hydroxyethyl starch vs pluronics, Mol. Pharm. 6 (2009) 407–415.
[23] S.H. Choi, J.-H. Lee, S.-M. Choi, T.G. Park, Thermally reversible pluronic/heparin nanocapsules exhibiting 1000-fold volume transition, Langmuir 22 (2006) 1758–1762.
[24] D. Cohn, H. Sagiv, A. Benyamin, G. Lando, Engineering thermoresponsive polymeric nanoshells, Biomaterials 30 (2009) 3289–3296.
[25] S. Stolnik, B. Daudali, A. Arien, J. Whetstone, C.R. Heald, M.C. Garnett, S.S. Davis, L. Illum, The effect of surface coverage and conformation of poly(ethylene oxide) (PEO) chains of poloxamer 407 on the biological fate of model colloidal drug carriers, Biochim. Biophys. Acta Biomembr. 1514 (2001) 261–279.
[26] S. Sun, H. Zeng, D.B. Robinson, S. Raoux, P.M. Rice, S.X. Wang, G. Li, Monodisperse MFe_2O_4 (M = Fe, Co, Mn) nanoparticles, J. Am. Chem. Soc. 126 (2003) 273–279.
[27] H.P. Martinez, Y. Kono, S.L. Blair, S. Sandoval, J. Wang-Rodriguez, R.F. Mattrey, A.C. Kummel, W.C. Trogler, Hard shell gas-filled contrast enhancement particles for colour Doppler ultrasound imaging of tumors, MedChemComm 1 (2010) 266–270.
[28] D.M. El-Sherif, M.A. Wheatley, Development of a novel method for synthesis of a polymeric ultrasound contrast agent, J. Biomed. Mater. Res. A 66A (2003) 347–355.
[29] H.-L. Liu, M.-Y. Hua, H.-W. Yang, C.-Y. Huang, P.-C. Chu, J.-S. Wu, I.-C. Tseng, J.-J. Wang, T.-C. Yen, P.-Y. Chen, K.-C. Wei, Magnetic resonance monitoring of focused ultrasound/magnetic nanoparticle targeting delivery of therapeutic agents to the brain, Proc. Natl. Acad. Sci. 107 (2010) 15205–15210.
[30] Y.-L. Chen, P.-C. Lin, S.-P. Chen, C.-C. Lin, N.-M. Tsai, Y.-L. Cheng, W.-L. Chang, S.-Z. Lin, H.-J. Harn, Activation of nonsteroidal anti-inflammatory drug-activated gene-1 via extracellular signal-regulated kinase 1/2 mitogen-activated protein kinase revealed a isochaihulactone-triggered apoptotic pathway in human lung cancer A549 cells, J. Pharmacol. Exp. Ther. 323 (2007) 746–756.
[31] R. Barreiro-Iglesias, L. Bromberg, M. Temchenko, T.A. Hatton, A. Concheiro, C. Alvarez-Lorenzo, Solubilization and stabilization of camptothecin in micellar solutions of pluronic-g-poly(acrylic acid) copolymers, J. Control. Release 97 (2004) 537–549.
[32] M.L. Fabiilli, K.J. Haworth, N.H. Fakhri, O.D. Kripfgans, P.L. Carson, J.B. Fowlkes, The role of inertial cavitation in acoustic droplet vaporization, IEEE Trans. Ultrason. Ferroelectr. Freq. Control 56 (2009) 1006–1017.
[33] S.B. Raymond, L.H. Treat, J.D. Dewey, N.J. McDannold, K. Hynynen, B.J. Bacskai, Ultrasound enhanced delivery of molecular imaging and therapeutic agents in Alzheimer's disease mouse models, PLoS One 3 (2008) 2175–2181.
[34] V. Frenkel, K.C.P. Li, Potential role of pulsed-high intensity focused ultrasound in gene therapy, Future Oncol. 2 (2006) 111–119.
[35] J.A. Poff, C.T. Allen, B. Traughber, A. Colunga, J. Xie, Z. Chen, B.J. Wood, C. Van Waes, K.C. Li, V. Frenkel, Pulsed high-intensity focused ultrasound enhances apoptosis and growth inhibition of squamous cell carcinoma xenografts with proteasome inhibitor bortezomib, Radiology 248 (2008) 485–491.
[36] P. Paparel, J.Y. Chapelon, A. Bissery, S. Chesnais, L. Curiel, A. Gelet, Influence of the docetaxel administration period (neoadjuvant or concomitant) in relation to HIFU treatment on the growth of Dunning tumors: results of a preliminary study, Prostate Cancer Prostatic Dis. 11 (2007) 181–186.
[37] E. Gultepe, F.J. Reynoso, A. Jhaveri, P. Kulkarni, D. Nagesha, C. Ferris, M. Harisinghani, R.B. Campbell, S. Sridhar, Monitoring of magnetic targeting to tumor vasculature through MRI and biodistribution, Nanomedicine 5 (2010) 1173–1182.

[38] R.D.K. Misra, Core–shell magnetic nanoparticle carrier for targeted drug delivery: challenges and design, Mater. Technol. Adv. Perform. Mater. 25 (2010) 118–126.
[39] Y. Yang, J.-S. Jiang, B. Du, Z.-F. Gan, M. Qian, P. Zhang, Preparation and properties of a novel drug delivery system with both magnetic and biomolecular targeting, J. Mater. Sci. Mater. Med. 20 (2009) 301–307.
[40] M. Arruebo, R. Fernández-Pacheco, M.R. Ibarra, J. Santamaría, Magnetic nanoparticles for drug delivery, Nano Today 2 (2007) 22–32.
[41] P.-Y. Chen, H.-L. Liu, M.-Y. Hua, H.-W. Yang, C.-Y. Huang, P.-C. Chu, L.-A. Lyu, I.-C. Tseng, L.-Y. Feng, H.-C. Tsai, S.-M. Chen, Y.-J. Lu, J.-J. Wang, T.-C. Yen, Y.-H. Ma, T. Wu, J.-P. Chen, J.-I. Chuang, J.-W. Shin, C. Hsueh, K.-C. Wei, Novel magnetic/ultrasound focusing system enhances nanoparticle drug delivery for glioma treatment, Neuro-Oncology 12 (2010) 1050–1060.
[42] V. Frenkel, Ultrasound mediated delivery of drugs and genes to solid tumors, Adv. Drug Deliv. Rev. 60 (2008) 1193–1208.